



# A phase-field approach for portlandite carbonation and application to self-healing cementitious materials

Sha Yang · Yangyiwei Yang · Antonio Caggiano · Neven Ukrainczyk · Eddie Koenders

Received: 21 June 2021 / Accepted: 7 January 2022  
© The Author(s) 2022

**Abstract** A conceptual phase-field model is proposed for simulating complex microstructural evolutions during the self-healing process of cementitious materials. This model specifically considers carbonation healing mechanisms activated by means of dissolution of soluble  $\text{Ca}(\text{OH})_2$  mineral and precipitation of the  $\text{CaCO}_3$  self-healing product. The system is described by a set of conservative and non-conservative field variables based on a thermodynamic analysis of the precipitation process and realised numerically using the finite element method (FEM). As a novel concept for modeling self-healing of cementitious materials, the evolution of multiple interfaces was investigated and demonstrated on a simple experimental test case of a self-healing mechanism consisting of carbonating calcium hydroxide. Parametric studies were performed to numerically investigate the effect of chemo-physical conditions. Two representative practical examples of

cementitious materials were numerically implemented. It is demonstrated that the simulated evolution of the crack morphology is in good qualitative agreement with the experimental data.

**Keywords** Self-healing · Phase-field method · Cementitious materials · Crack morphology · Dissolution · Precipitation

## 1 Introduction

The problem of cracks in cementitious materials is a widespread and thorough engineering problem [1]. Although small cracks do not directly cause structural failure, they can also accelerate the deterioration of a structure [2]. The presence of cracks not only affects the permeability of building structures and reduces their freeze–thaw resistance, but also many enhance the chloride attack of concrete [3–6]. Inspired by nature, a variety of self-healing mechanisms have been developed for cementitious materials [7–11], which has led to concrete materials becoming intelligent and capable of detecting the damage and repairing themselves. According to the report RILEM TC-221-SHC, the self-healing mechanism can be classified into “autogenic” and “autonomic” [12]. The autogenous self-healing is mainly based on the original composition of cementitious materials, which consists of three

---

S. Yang · A. Caggiano (✉) · N. Ukrainczyk · E. Koenders  
Institute of Construction and Building Materials,  
Technical University of Darmstadt, 64287 Darmstadt,  
Germany  
e-mail: caggiano@wib.tu-darmstadt.de

Y. Yang (✉)  
Mechanics of Functional Materials Division, Institute of  
Materials Science, Technical University of Darmstadt,  
64287 Darmstadt, Germany  
e-mail: yangyiwei.yang@mfm.tu-darmstadt.de



mechanisms: (1) the cement matrix on the crack surface absorbs water leading to volume expansions [12], (2) further hydration of the unhydrated cement clinker [13], and (3) carbonation of the additionally formed portlandite [14]. The autonomous self-healing is carried out with the help of healing agents. Depending on its composition, the healing agent can be divided into polymers [15], minerals [16] and bacterial spores [17].

The currently available numerical methods for self-healing can be grouped according to the nature of their self-healing mechanisms into: (1) chemical reaction-based models, for predicting carbonation [18], further hydration [13, 19–25], precipitation [26, 27] and encapsulation [28–31]; and (2) transport-based models [18, 27], in which the phases affecting the healing processes are transported through the pore-structure network. A few models involve thermodynamics. Huang and Ye [32] modeled the further hydration of unhydrated cement particles based on a thermodynamic-diffusion model with coupled mass balance, charge balance and chemical equilibrium. In addition, Lattice–Boltzmann Method (LBM) as a class of computational fluid dynamics (CFD) methods for fluid simulation has been used for self-healing materials in non-equilibrium thermodynamic states, such as polymer [33] and cementitious materials [34]. For the carbonation reaction, which is one of the important mechanisms of self-healing in cementitious materials, there are numerous studies that consider it as a moving boundary problem since the position of the free boundary is a function of time [35–38].

Based on the present literature review, it can be summarized that self-healing of cementitious materials is treated analytically and numerically mainly using reaction–diffusion equations. However, these models have several limitations. Firstly, the solid–liquid interface is treated as a sharp interface, which leads to the discontinuity in some of the continuously varying parameters at the interface (e.g. ionic concentration field), making it difficult to trace the evolution of certain physical processes, notably, the concentration profile across the interface. Secondly, sharp interfaces have to be explicitly tracked, especially for the evolution of high-dimensional, microstructurally complex interfaces, which can make numerical calculations extremely difficult. Thirdly, only single solid–liquid interface has been investigated in existing models. The effect of dissolution of

soluble minerals on the fracture surface on the initial solid-phase boundary is not yet considered. Finally, these models are concentrated solely on the standalone self-healing process, neglecting interactions between the concentration of aqueous species in the solution, the moving front of self-healing products, and the morphology of the interface. The above limitations will be overcome by applying the phase-field (PF) method presented in this study.

The PF method provides an effective way to simulate migration problems of thermodynamically driven interfaces, which applies order parameters (OPs) to represent microstructures (e.g. pores, liquid and solid phases) and can include natural thermodynamic quantities such as concentration and temperature. The OPs take different constant values in different regions and have a continuous spatial variation across the interface. The microstructure and its evolution is thus reproduced by the spatial and temporal distribution of the OPs, without the need for interfacial tracking [39]. Several PF models for dissolution and/or precipitation simulations have been proposed: solutes in liquids [40–42], tri phases in porous media (two immiscible fluids and a solid phase) [43], binary or ternary alloys [44–46]. Moreover, some PF models for simulating metal corrosion are also worthy of reference [47–49].

Unlike the conventional sharp and/or single interface PF models, the contribution of presented novel PF model is based on thermodynamics to simulate the evolution of multi diffusion interfaces of self-healing process. We used the physicochemical principles of the self-healing problem to construct a free energy function that incorporates the mechanism of dissolution and precipitation interactions. By introducing an auxiliary (phase) field as a front tracking tool, the complex interface migration are implicitly solved. Specifically, the solution of the model consists of determining the concentration fields of the active species and the PF.

Based on the above overview, this study will report numerical simulations of the carbonation reaction of cementitious materials using the PF method from the perspective of dissolution and precipitation. The numerical model is introduced in Sect. 2, including the novelty on the construction of energy functions for multiphase dissolution and precipitation. Numerical simulation and experimental methodology is presented in Sect. 3. The experimental validation and

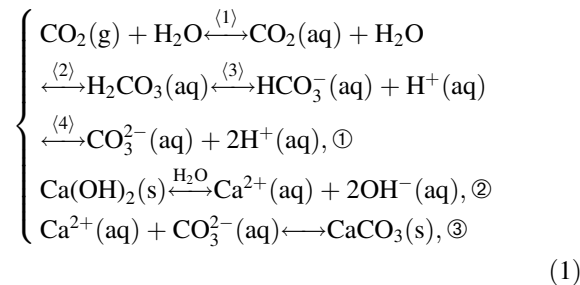


the model application are demonstrated in Sect. 4, followed by a series of parametric studies. Finally, concluding remarks are provided in Sect. 5.

## 2 Phase-field model of self-healing

### 2.1 Phase-field scenario

From a chemical point of view, the hydration reaction of cementitious materials is a complex dissolution–precipitation reaction in which, unlike the reaction of a single component, numerous components of cementitious materials react simultaneously with different thermodynamics and kinetics, and the various mineral components interact with each other. This poses a great challenge for modeling. However, the carbonation reaction, which is one of the main mechanisms of self-healing in cementitious materials, could be simplified as a  $\text{Ca}(\text{OH})_2$  dissolution and  $\text{CaCO}_3$  precipitation process. From the modeling point of view, a simplified approach to the analysis of the carbonation reaction (Eq. 1) [35, 50] can help to analyze and understand the complex self-healing mechanism based on nonequilibrium thermodynamics.



where “aq”, “g” and “s” refer to species which are in an aqueous, gaseous and solid states, respectively.

Figure 1 shows the carbonation process and the corresponding profiles of the OPs in the PF model. Generally, the carbonation based self-healing consists of three main mechanisms: (1)  $\text{CO}_2$  dissolves in water to form carbonate ions, (2) dissolution of  $\text{Ca}^{2+}$  ions source phase  $\text{Ca}(\text{OH})_2$ , hydration product, e.g. calcium silicate hydrate ( $\text{C-S-H}$  or  $3\text{CaO} \cdot 2\text{SiO}_2 \cdot 3\text{H}_2\text{O}$ ) and non-hydrated cement phases, e.g. tricalcium silicate ( $\text{C}_3\text{S}$  or  $3\text{CaO} \cdot \text{SiO}_2$ ) and dicalcium silicate ( $\text{C}_2\text{S}$  or  $2\text{CaO} \cdot \text{SiO}_2$ ) [51] in the unsaturated solution, and (3) nucleation and growth of precipitated  $\text{CaCO}_3$  in the supersaturated solution

[52]. The dissolution of  $\text{CO}_2$  (g) in water proceeds through a multi-step equilibrium reactions (mechanism 1, reaction (1)), where the reaction (2) is the bottleneck process, as only a very small fraction of  $\text{CO}_2$  (aq) is transformed into  $\text{H}_2\text{CO}_3$ . In our first PF approach, a full availability of  $\text{CO}_3^{2-}$  species is considered, thus neglecting the kinetic effects of  $\text{CO}_2$  dissolution steps (1)–(4). A more detailed modeling approach for the carbonation of cement pastes considering chemical thermodynamics and diffusive and convective transports can be found in recent literature, e.g. [53]. Following the PF scenario, the ion diffusion in each phase (labeled as  $i$ ) is described with a conserved field variable, i.e.  $c_i$  adopting physical meaning of the concentration and track the phase evolution with a non-conserved field variable, i.e.  $\phi_i$  adopting the physical meaning of the volumetric fraction of the phase  $i$ . Note here the  $c_i$  refers to the ratio of the actual ionic concentration  $C_i$  at a certain position and time to the initial concentration of the source phase  $C_{\text{SOU}}^0$ , both in units of  $\text{mol}/\text{m}^3$  (see Table 1, Sect. 3.1.2). The calcium ion source phase  $\phi_{\text{SOU}}$  (hereafter referred to as the source phase), the precipitation phase  $\phi_{\text{PRE}}$  and the aqueous solution phase  $\phi_{\text{AQ}}$  together form a multiphase system.

In the initial stage ( $0 < t < t_p$ ), when the dissolution begins, i.e., only  $\phi_{\text{SOU}}$ ,  $\phi_{\text{AQ}}$  and their interface  $I_{\text{a-s}}$ , are present in the system. Then  $\text{Ca}^{2+}$  ions diffuse from  $\text{Ca}(\text{OH})_2$ , hydration products and unhydrated cement particles ( $t > t_p$ ), and react with dissolved  $\text{CO}_2$  in water to form suspended  $\text{CaCO}_3$ . As its concentration reaches a saturation  $c_{\text{AQ}}^{\text{E}}$  and even an oversaturation state  $c_{\text{AQ}}^{\text{sat}}$ , calcium carbonate pre-nucleates, nucleates, and eventually later forms crystals, precipitating on the crack surface. The interaction energy of  $\text{CaCO}_3$  particles is strongly dependent on the ionic concentration in the solution [54]. This is mainly due to the fact that  $\text{Ca}^{2+}$  ions in solution produce short-range attractive and long-range repulsive interactions [55].  $\text{CaCO}_3$  particles accumulate more in ion-concentration-enriched regions. Therefore, the ion concentration can be used to express the local packing density of precipitated  $\text{CaCO}_3$  particles. The corresponding interfaces of  $\phi_{\text{PRE}}$  with  $\phi_{\text{SOU}}$  and  $\phi_{\text{AQ}}$  are denoted by  $I_{\text{s-p}}$  and  $I_{\text{p-a}}$ , respectively.

Based on the self-healing mechanism described above, several modeling assumptions have been made:



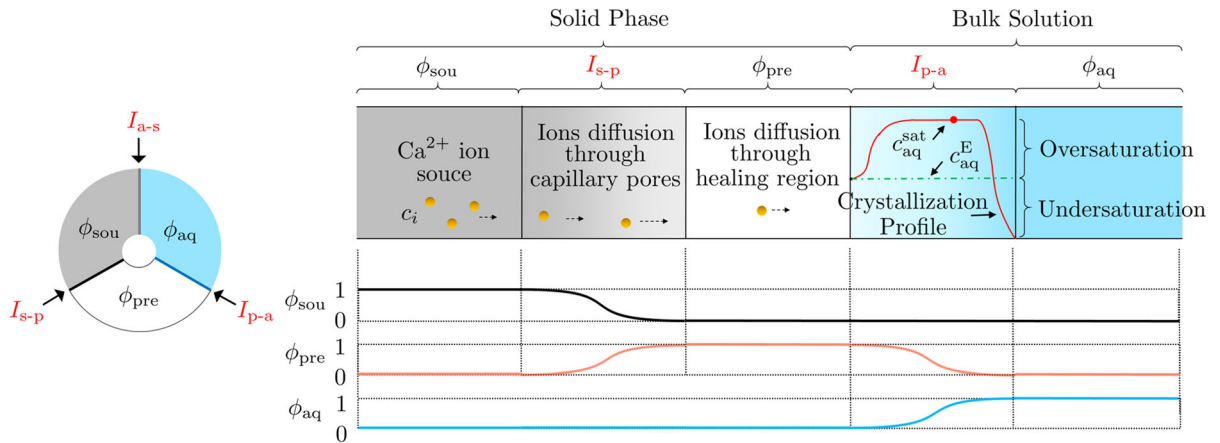


**Fig. 1** Schematic diagram of the simplified self-healing mechanism and profiles of the order parameters of the corresponding phases;  $t_p$  is the time to start precipitating

**Table 1** The dimensionless forms of the parameters

	Symbol	Normalization		Symbol	Normalization
Physical quantity	$c_i$	$c_i^* = C_i/C_{\text{sou}}^0$	Model parameter	$A_i$	$A_i^* = A_i/\omega_{\text{pre}}$
	$L_i$	$L_i^* = \omega_{\text{pre}} r^2 L_i / (D_{\text{aq}})$		$\omega_i$	$\omega_i^* = \omega_i / \omega_{\text{pre}}$
	$t$	$t^* = D_{\text{aq}} t / r^2$		$\kappa_i$	$\kappa_i^* = \kappa_i / (\omega_{\text{pre}} r^2)$
	$D_i$	$D_i^* = D_i / (D_{\text{aq}})$			
Operators	$\nabla$	$\nabla^* = r \nabla$			

- only the reaction of  $\text{Ca}^{2+}$  with  $\text{CO}_3^{2-}$  ions to form  $\text{CaCO}_3$  is considered. The carbonation products do not contain other intermediate substances;
- all  $\text{Ca}^{2+}$  ions localized in the crack solution may eventually be equilibrated with respect to  $\text{CaCO}_3$  precipitates;
- since the number of moles of  $\text{CaCO}_3$  is the same as that of  $\text{Ca}^{2+}$  ions it contains, the diffusion of all aqueous species ( $\text{Ca}^{2+}$  ions and suspended  $\text{CaCO}_3$ ) can be expressed as a single ionic concentration  $c_i$ ;
- the diffusion coefficients of aqueous substances in phase ( $\phi_{\text{pre}}$ ,  $\phi_{\text{sou}}$  and  $\phi_{\text{aq}}$ ) and the corresponding interface ( $I_{\text{s-p}}$  and  $I_{\text{p-a}}$ ) are constant, respectively (see Fig. 1).

## 2.2 Thermodynamic and kinetic formulations

The multi non-conserved OPs  $\{\phi_i\}$  are continuous functions of time  $t$  and space  $x$ , which indicate each

phase to convert between 0 and 1 within a thin diffusion transition interface. Subscription  $i = \text{sou}, \text{pre}$  and  $\text{aq}$  is used further. The three phase contributions ( $\phi_{\text{sou}}$ ,  $\phi_{\text{pre}}$  and  $\phi_{\text{aq}}$ ) are constrained following [56], i.e.,

$$\phi_{\text{sou}} + \phi_{\text{pre}} + \phi_{\text{aq}} = 1. \quad (2)$$

Considering this multi-phase constraint, the free energy  $\mathcal{L}$ , within the simulation domain  $\Omega$  with the Lagrangian multiplier  $\lambda$ , is written as

$$\begin{aligned} \mathcal{L}(\{c_i\}, \{\phi_i, \nabla \phi_i\}) = & \int_{\Omega} [f_{\text{loc}}(\{c_i\}, \{\phi_i\}) \\ & + f_{\text{int}}(\{\nabla \phi_i\}) \\ & + \lambda(1 - \sum \phi_i)] d\Omega, \end{aligned} \quad (3)$$

where  $f_{\text{loc}}$  and  $f_{\text{int}}$  are the terms for local and interface free energy density, respectively. The local free

energy  $f_{1OC}$  can be formulated as an extension of the double-well function as

$$f_{1OC}(\{c_i\}, \{\phi_i\}) = \sum_i [\Phi_i(\phi_i)f_i(c_i) + \omega_i g(\phi_i)] \quad (4)$$

where  $\Phi_i(\phi_i)$  are originally the tilting functions [57], which is reduced in this work in a two-phase interpolating function as:  $\Phi_i(\phi_i) = (10 - 15\phi_i + 6\phi_i^2)\phi_i^3$ .  $\omega_i$  is the height of the imposed double-well energy barrier of each phase.  $g(\phi_i) = \phi_i^2(1 - \phi_i)^2$  is the double-well potential. The free energy density of each phase  $f_i(c_i)$  is approximated by a parabolic function as follows

$$f_{sou}(c_{sou}) = A_{sou}(c_{sou})^2, \quad (5)$$

$$f_{pre}(c_{pre}) = A_{pre}(c_{pre} - c_{pre}^E)^2 - \Delta_r f, \quad (6)$$

$$f_{aq}(c_{aq}) = A_{aq}(c_{aq} - c_{aq}^E)^2, \quad (7)$$

where  $A_i$  is the potential parameter employed to construct the local free energy of distinct phases in order to approximate the actual thermodynamic system.

Figure 2 illustrates the path of local free energy variation with the concentration  $\{c_i\}$  and the order parameters  $\{\phi_i\}$  for the three stages of the self-healing reaction, i.e. (0) undersaturation, (1) saturation and (2)

oversaturation. In the unsaturated state,  $Ca^{2+}$  ions dissolve from the cementitious matrix and diffuse into the solution to form suspended  $CaCO_3$ , which is accompanied by a decrease in the solute concentration in the cementitious matrix from  $c_{sou}^{(0)}$  to  $c_{sou}^{(1)}$  and an increase in the solute concentration from  $c_{aq}^{(0)}$  to  $c_{aq}^{(1)}$  in the solution. The difference in the diffusion energy of the cementitious matrix changes from  $\Delta_{dis}f^{(0)}$  to  $\Delta_{dis}f^{(1)}$ . The precipitation chemical driving force  $\Delta_{pref}^{(0)}$  is negative when the solution is not saturated, which corresponds to the inability to precipitate but only to dissolve. When the solution is saturated or even supersaturated ( $c_{sou}^{(1)}$  to  $c_{sou}^{(2)}$  and  $c_{aq}^{(1)}$  to  $c_{aq}^{(2)}$ ), i.e. the chemical driving force  $\Delta_{pref}^{(2)}$  is positive, after which the suspended  $CaCO_3$  starts to precipitate. In order to properly emulate this process,  $A_{sou} < A_{aq} \ll A_{pre}$  should be numerically satisfied. Meanwhile, the thermodynamic driving force for the precipitation of  $CaCO_3$  consists of the contribution of the reaction part  $\Delta_r f^{(2)}$  and the diffusion part  $\Delta_{dif}f^{(2)}$ .

The precipitation follows a non-equilibrium process in which  $CaCO_3$  aggregates with characteristic mean cluster size form and grow, thus filling the cracks. For  $CaCO_3$  nanoparticles present in solution, their mutual clustering is strongly dependent on the ionic concentration of the solution. When the ionic

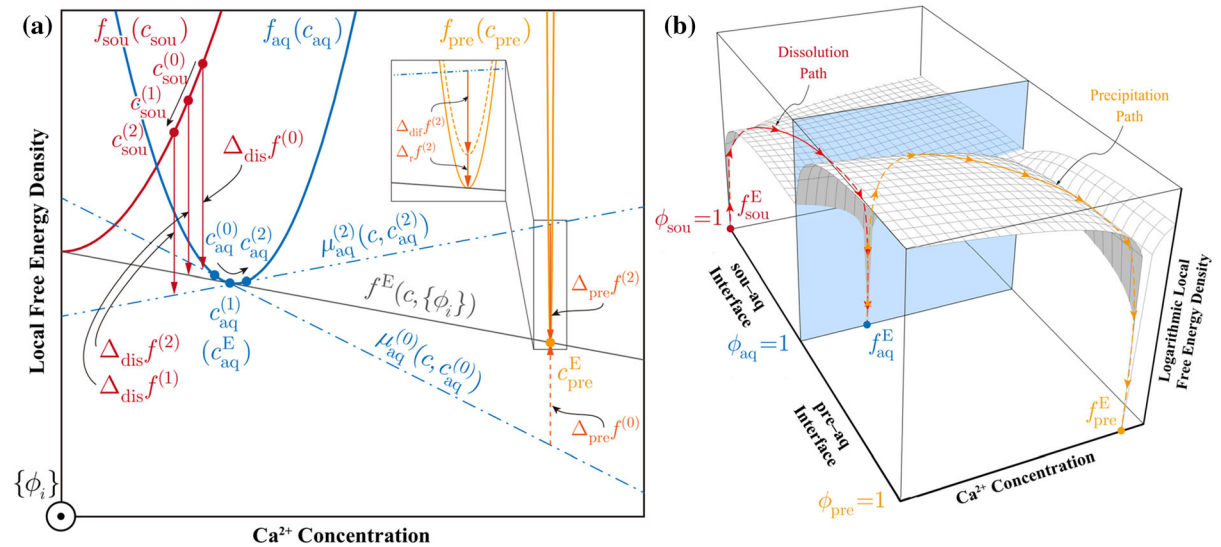


**Fig. 2** a Processes and driving forces for the three stages. b Logarithmic free energy density landscape among the source phase, the precipitation phase, and the aqueous solution as the

junction phase. Energy variation paths (of dissolution and precipitation) are also illustrated

concentration is small, dissolution of the reactants is promoted. An increase in the ionic concentration rapidly promotes the production of more precipitation. The precipitation reaction term  $\Delta_{\Gamma} f$  should be an expression of the free energy density related to the chemical formation of  $\text{CaCO}_3$  particles [58]. In this PF model, we simplify the precipitation term to a non-negative constant. With this constant we are able to define the free energy of the precipitation phase  $f_{\text{pre}}(c_{\text{pre}})$  (as shown in Eq. 6) in the region that allows the  $\text{CaCO}_3$  precipitation, i.e. located in the oversaturation (OS) regions.

The energy contributions at the diffusive interface is formulated [59] as

$$f_{\text{int}}(\nabla\{\phi_i\}) = \sum_i \frac{\kappa_i}{2} |\nabla\phi_i|^2 \quad (8)$$

where  $\kappa_i$  is the gradient energy coefficient of each phase. Based on the formulations of [59], the interface is described as a mixture of multi-phase with different compositions, but with the same chemical potential. The local concentration  $c$  is thus defined as the weighted superposition of each phase  $c_i$

$$c = \Phi_{\text{sou}} c_{\text{sou}} + \Phi_{\text{pre}} c_{\text{pre}} + \Phi_{\text{aq}} c_{\text{aq}}. \quad (9)$$

These phase concentrations are further constrained by an equal-chemical-potential condition, i.e.

$$\mu = \frac{\partial f_{\text{sou}}}{\partial c_{\text{sou}}} = \frac{\partial f_{\text{pre}}}{\partial c_{\text{pre}}} = \frac{\partial f_{\text{aq}}}{\partial c_{\text{aq}}}. \quad (10)$$

The temporal evolution of the non-conserved order parameters  $\{\phi_i\}$  is governed by the Allen–Cahn equation [60] as

$$\frac{\partial \phi_i}{\partial t} = -L_i \frac{\delta \mathcal{L}}{\delta \phi_i} \quad (11)$$

with the corresponding interface mobility coefficient  $L_i$ . On the other hand, the conserved local concentration field  $c$  is governed by diffusion equation [59] as

$$\frac{\partial c}{\partial t} = \nabla \cdot \left( D \sum_i \Phi_i \nabla c_i \right), \quad (12)$$

which can be also regarded as the reduced version of Cahn–Hilliard equation by applying the chain rule on the chemical potential [59]. The solute diffusion coefficient can be formulated as  $D = \sum_i \Phi_i D_i$

considering the effective value of each phase  $D_i$  and corresponding interpolation  $\Phi_i$ .

Analyzing the equilibrium properties of the kinetic equations (11) and (12) by means of the thin interface limit analysis [59], the unknown model parameters  $\kappa_i$  and  $\omega_i$  can be expressed by the interfacial energy  $\sigma_{i-j}$  and the interfacial width  $l_{i-j}$ . As the general formation,  $\kappa_i$  and  $\omega_i$ , corresponding to the OP  $\phi_i$ , are calculated as follows

$$\kappa_i = \frac{3}{4} (\sigma_{i-j} l_{i-j} + \sigma_{i-k} l_{i-k} - \sigma_{j-k} l_{j-k}), \quad (13)$$

$$\omega_i = 6 \left( \frac{\sigma_{i-j}}{l_{i-j}} + \frac{\sigma_{i-k}}{l_{i-k}} - \frac{\sigma_{j-k}}{l_{j-k}} \right), \quad (14)$$

where  $i, j, k$  are distinct phase subscriptions, i.e. sou, pre or aq.

### 3 Method

#### 3.1 Numerical method

##### 3.1.1 Simulation setup

Figure 3 shows a 2D schematic view of a simulation domain of size  $375 \mu\text{m} \times 750 \mu\text{m}$  for the parameter research. The initial width of the crack is set to  $150 \mu\text{m}$ . In this model, the solid calcium hydroxide provides a source of calcium ions. When the crack width is much smaller than the size of the source phase and the number of cracks is sufficiently few, it can be considered as a constant supply of calcium ions in the system. However, when the cracks are densely

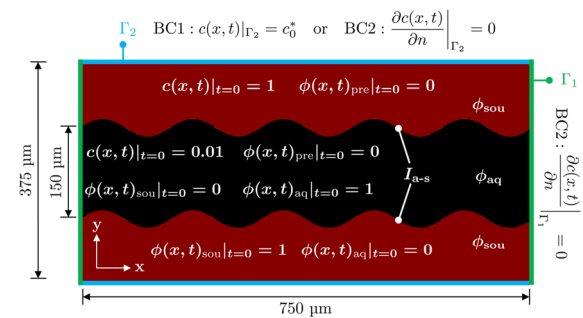


**Fig. 3** Schematic view of a typical crack and the initial and boundary conditions used in the PF model. The source phase and the aqueous solution phase are separated by the diffusion interface  $I_{a-s}$

distributed, this causes competition for the supply of  $\text{Ca}^{2+}$  ions around the cracks. Therefore, only a limited ions supply is available. This phenomenon can be simulated by two boundary conditions (BC), i.e. BC1: the boundary of the domain  $\Gamma_1$  is a constant concentration ion reservoir following (Eq. 9); BC2: there is no mass exchange between the domain and the environment along the outward unit normal of the boundary  $\Gamma_2$ .  $\mathbf{n}$  is the normal vector. For the realistic simulation of the model, binary large objects (BLObs) were converted from the experimental images derived from the stereo microscope (see Sect. 4.3), imported and processed using the MOOSE-embedded ImageFunction and associated utilities.

### 3.1.2 Parameter normalization

To ensure the convergence of the model and to improve the computational efficiency of solving the non-linear governing equation sets, all variables are normalized. Spatial derivatives are normalized with respect to the reference length  $r$ , which is set to 5% of the initial crack width. Dimensionless forms of other quantities are given in Table 1.

In order to enable a valid comparison of the varying order parameters in the same time frame, the original data were linearly transformed by equation 15.

$$\phi_i^* = \frac{\phi_i^t - \phi_i^{\min}}{\phi_i^{\max} - \phi_i^{\min}} \quad (15)$$

where  $\phi_i^t$  is the integration of the corresponding phase at the time  $t$  over the 2D domain, while  $\phi_i^{\min}$  and  $\phi_i^{\max}$  represent the minimum and maximum integration of the corresponding phase, respectively. The residual source phase ratio, the precipitation generation ratio and the self-healing ratio can be expressed as the corresponding normalized phase ratio  $\phi_{\text{sou}}^*$ ,  $\phi_{\text{pre}}^*$  and  $\phi_{\text{aq}}^*$ , respectively. The physical meaning for the integration, could be related in terms of the derivative of the porosity integral on the surface.

### 3.1.3 Finite element implementation

The PF model was implemented using the finite element method (FEM) in the framework of the multiphysics object-oriented environment (MOOSE) [61]. 4-node quadratic Lagrangian elements were

chosen to mesh the geometry. Transient solver with preconditioned Jacobian-Free Newton–Krylov method (PJFNK) and backward Euler algorithm were employed. Adaptive mesh and time stepping schemes are used to reduce computation costs. Error indicators employed in H-adaptive meshing scheme on both  $\{\phi_i\}$  and  $\{c_i\}$ , with the  $h$ -level as four, were specified to guarantee the precision requirement of the diffusive interface.

## 3.2 Experimental method

Experimental studies were conducted at the Institute of Construction and Building Materials of the TU Darmstadt. The  $\text{Ca}(\text{OH})_2$  powder (ROTH, >96%) was compressed by a hydraulic press (ENERPAC P142, USA) at 40 MPa pressure into tablet specimens having dimensions of 15 mm diameter and 10 mm height (Fig. 4). The specimens were completely sealed using a vacuum impregnation device (EPOFIX from Struers, Denmark) at a pressure of 20 kPa then a fissure opening with a width of 1.0 mm was carved along its diameter. This geometry was chosen to ensure one dimensional advancement of the carbonation reaction front. Each specimen was immersed in 200 mL distilled water and transferred to a regulated environmental chamber (ICH-C 110, Memmert, Germany) and carbonized for 3, 7, 14 and 21 days at a temperature of 20 °C, a relative humidity of 80% (to avoid the evaporation of water from the vessel).

Due to the low concentration of  $\text{CO}_2$  in the atmosphere (about 0.03% by volume), the carbonation process of  $\text{Ca}(\text{OH})_2$  and cementitious materials is very slow in the natural environment. Accelerated carbonation experiments are usually performed in the laboratory to quickly assess the carbonation process. In the literature, the  $\text{CO}_2$  concentration for accelerated carbonation varies from 3 to 100% [62, 63]. The carbonation rate increases with increasing  $\text{CO}_2$  concentration. However, this development is not significant at  $\text{CO}_2$  concentrations above 20%, due to the fact that at high  $\text{CO}_2$  concentrations, in the outer layers of the concrete, dense carbonation microstructures are formed, which prevent further penetration of  $\text{CO}_2$  [64]. In order to ensure that the accelerated carbonation produces a sustained self-healing effect, a  $\text{CO}_2$  concentration of 5% by volume was chosen for this study. Here it is important to note that our model disregarded the  $\text{CO}_2$  dissolution kinetics, by assuming

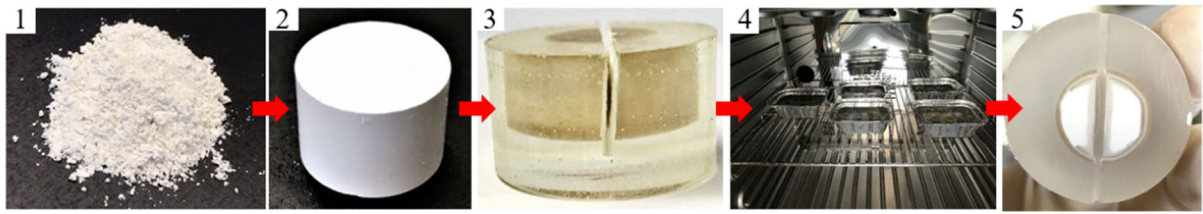


**Fig. 4** Schematic procedure of  $\text{Ca}(\text{OH})_2$  carbonation experiments

that the  $\text{CO}_3^{2-}$  is fully available in the pore system, i.e. the dissolution kinetics is instantaneous. In future modeling works, the  $\text{CO}_2$  dissolution kinetics should be considered as well.

At each exposure time period, the corresponding specimen was taken out of the water and dried at  $40^\circ\text{C}$  for 24 h. The crack opening was then vacuum filled with a low viscosity (nominally 0.6 mPa s) epoxy resin. After the epoxy resin hardened, the specimens were polished using a semi-automatic grinding–polishing machine (LaboSystem, Struers, Denmark), initially using a disc in hardness range HV 150–2000 at a rotational speed of 300 rpm, followed by a lubricated cloth and polycrystalline diamond spray of, consecutively, 9, 3, and  $1\ \mu\text{m}$  sizes at a rotational speed of 150 rpm. The polished cross-sections of the specimens were imaged by an environmental scanning electron microscopy using a back-scattered electron detector (SEM-BSE, Zeiss EVO LS25, Germany). The chemical analysis of the polished cross sections of the samples were conducted using the energy dispersive spectroscopy (EDS) detector.

## 4 Results and discussion

### 4.1 Experimental validation

The purpose of the experimental observation of the carbonation reaction of a single substance,  $\text{Ca}(\text{OH})_2$ , is to verify the appropriateness of the multiple interfaces settings in the PF model. Figure 5a shows the SEM images of specimens after different repair time. The dashed line indicates the initial solid–liquid interface  $I_{a-s}$ . The dissolution process of calcium hydroxide occurs first on the exposure surface. As the solution penetrates the surface layer of  $\text{Ca}(\text{OH})_2$  is exfoliated. By day 7, typical dendritic calcium carbonate crystals can be clearly observed on the

stripped layer. Based on this dendritic layer of  $\text{CaCO}_3$  crystals,  $\text{CaCO}_3$  will continue to precipitate and fill the voids, resulting in a porous layer. The pore system provides a channel for further bi-directional diffusion of  $\text{CO}_3^{2-}$  and  $\text{Ca}^{2+}$  ions. By day 14 it can be seen that the carbonate ions diffuse through the porous  $\text{CaCO}_3$  layer generated at the crack surface into the  $\text{Ca}(\text{OH})_2$  matrix and undergo precipitation reactions, which allows the interface  $I_{s-p}$  to continue to move deeper into the matrix. At the same time, the interface  $I_{p-a}$  continued to grow toward the solution, and by day 21, the cracks had completely healed. Non-homogeneously distributed light-colored patches in the healed regions were observed in the SEM images, which was due to the studied cross-section of the precipitation region containing crystalline  $\text{CaCO}_3$  [65]. We also analysed the different depths of the cracks in combination with stereo microscopy and found that in the 21-day sample, the deeper areas of the cracks were completely filled with calcium carbonate.  $\text{CaCO}_3$  composition was confirmed using EDS point analysis (average composition of 40.05 wt% Ca, 15.71 wt% C, 44.24 wt% O, Fig. 5c). From the experimental results in Fig. 5b, it can be seen that by 21 days, the total moving distance of single side of  $I_{p-a}$  is 2.7 times greater than that of  $I_{s-p}$ .

The experiment results also showed that  $I_{s-p}$  receded rapidly during the first 7 days of the experiment and moved slowly thereafter. The reason for this phenomenon is that the solute concentration of the exposed solution is zero (initial condition), i.e. the diffusion flux is initially very high. This leads to a rapid retreat of the interface due to the continuous dissolution controlled by  $L_{\text{Sou}}$ . As the precipitation reaction continues on the fracture surface, a structurally dense  $\text{CaCO}_3$  layer is formed, which prevents the penetration of  $\text{CO}_3^{2-}$  ions into  $\text{Ca}(\text{OH})_2$  matrix on the one hand, and the leaching of  $\text{Ca}^{2+}$  ions into the solution on the other hand. This rate of interface



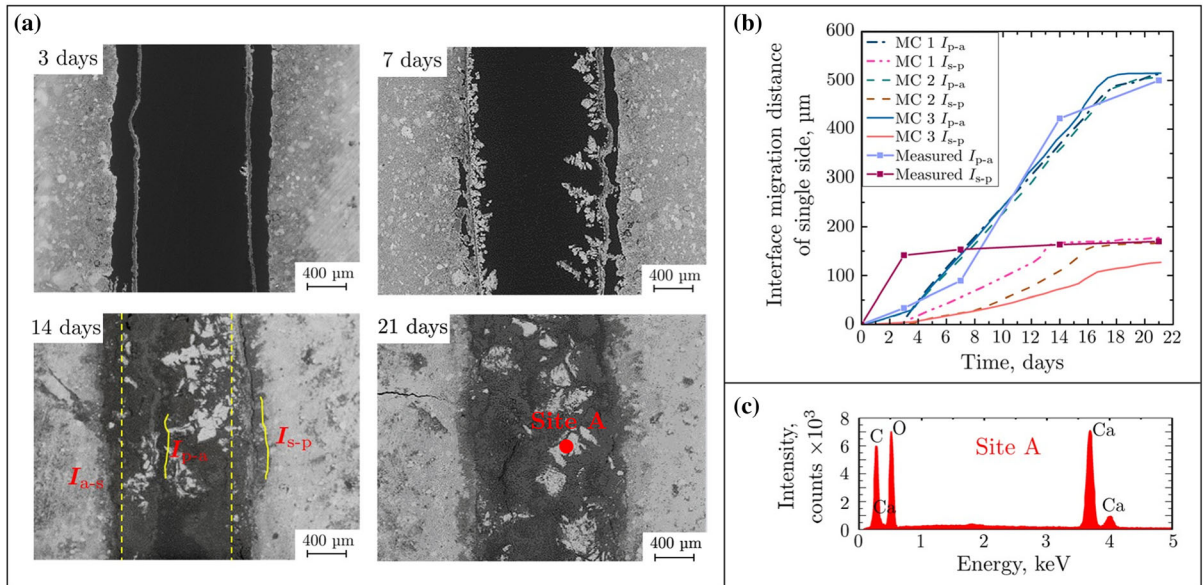


**Fig. 5** Image and data analysis of the interfacial migration of Ca(OH)<sub>2</sub> carbonation over time. **a** SEM image after different self-healing exposure times, i.e. 3, 7, 14 and 21 days;

**b** comparison of numerical and experimental results of the interface migration distance, model case is abbreviated as MC and **c** the EDS spectrum of the self-healing product

migration in the PF model may be considered in the future in  $L_{SOU}$ , where this mobility should vary with time and is fundamentally a function of solute concentration and porosity. However, in this study,  $L_{SOU}$  is simplified to a constant. The effects of varying  $L_{SOU}$  (case 1, 2, and 3) on the evolution of  $I_{s-p}$  are compared with the experimental results.

The migration distances of the single side of  $I_{p-a}$  and  $I_{s-p}$  are calculated from the integration lengths of  $\phi_{aq}$  and  $\phi_{SOU}$  in the 1D simulation, respectively. The model parameters for case 1 are summarized in Table 2.

The parameter  $A_i$  is taken to construct the free energy of the cementitious system (Fig. 2). The interface mobility coefficient  $L_i$  is related to the interface velocity and the driving force according to the chemical rate theory. In most of the studies, the values of interface mobility are used as empirical or hypothetical ones [49, 66]. In our study, the interface mobility was determined based on experiment results. For case 2 and case 3,  $L_{SOU}$  has the value of  $5 \times 10^{-5}$  and  $3.5 \times 10^{-5}$ , respectively. Other parameters are the same as that of case 1.  $c_{aq}^E$  is derived from the solubility of CaCO<sub>3</sub> at 20 °C and 1 atm.  $c_{pre}^E$  is the

**Table 2** Model parameters

Symbol	Value	Unit	Symbol	Value	Unit	References
$A_{sou}$	$2.40 \times 10^{-5}$	J/m <sup>3</sup>	$\kappa_{pre}$	$7.24 \times 10^{-9}$	J/m	
$A_{pre}$	$2.40 \times 10^{-2}$	J/m <sup>3</sup>	$\kappa_{aq}$	$1.76 \times 10^{-9}$	J/m	
$A_{aq}$	$2.40 \times 10^{-4}$	J/m <sup>3</sup>	$\sigma_{s-p}$	$2.11 \times 10^{-4}$	J/m <sup>2</sup>	[70]
$\omega_{sou}$	27.48	J/m <sup>3</sup>	$\sigma_{p-a}$	$1.20 \times 10^{-4}$	J/m <sup>2</sup>	[70]
$\omega_{pre}$	23.16	J/m <sup>3</sup>	$\sigma_{a-s}$	$1.38 \times 10^{-4}$	J/m <sup>2</sup>	[71]
$\omega_{aq}$	5.64	J/m <sup>3</sup>	$D_{sou}$	$1.34 \times 10^{-14}$	m <sup>2</sup> /s	
$L_{sou}$	$7.00 \times 10^{-5}$	m <sup>2</sup> /(Js)	$D_{pre}$	$5.40 \times 10^{-12}$	m <sup>2</sup> /s	[72]
$L_{pre}$	$1.80 \times 10^{-4}$	m <sup>2</sup> /(Js)	$D_{aq}$	$1.34 \times 10^{-9}$	m <sup>2</sup> /s	[73]
$L_{aq}$	$1.80 \times 10^{-4}$	m <sup>2</sup> /(Js)	$c_{pre}^E$	$1.35 \times 10^4$	mol/m <sup>3</sup>	
$\kappa_{sou}$	$8.59 \times 10^{-9}$	J/m	$c_{aq}^E$	$1.40 \times 10^{-1}$	mol/m <sup>3</sup>	[74]

molar concentration of the calcium ion of  $\text{CaCO}_3$  with a porosity of 47%.  $C_{\text{SOu}}^0$  is calculated by dividing the density of  $\text{CaCO}_3$  by its average molar mass [67]. The porosity of the diffusion coefficient of the source phase  $D_{\text{SOu}}$  is obtained from the compaction density and the particle density of  $\text{Ca}(\text{OH})_2$  specimens, i.e. 30%. Based on the relationship between the diffusion coefficient, the open porosity and the pore morphology [68, 69],  $D_{\text{SOu}}$  is set to be 5 orders of magnitude smaller than in its solution. As this is a crack scale model, it operates both with ion diffusivity in pore (crack) solution and effective diffusivity through porous matrix. The value of  $D_{\text{pre}}$  was determined by choosing the ion diffusion coefficient of a cementitious material with approximate porosity to the precipitated phase.

Figure 5b shows that the profiles of  $I_{\text{p-a}}$  in the three cases were in good agreement with the experimental results, although the measured value on day 7 is slightly lower than that of the simulation where the measured value on day 14 is higher than the simulated values. The results for the three models cases show a slowdown in the rate of interface migration after day 16, which is consistent with the results of the parametric analysis in Fig. 6a in Sect. 4.2. For the evolution of  $I_{\text{s-p}}$  it can be seen that for an increasing  $L_{\text{SOu}}$ , it is possible to facilitate the  $I_{\text{s-p}}$  migration in case 1 ( $7 \times 10^{-5}$ ) and case 2 ( $5 \times 10^{-5}$ ) and to make the total distance consistent with the experiments. However, the backward distance of  $I_{\text{s-p}}$  grows rapidly during the first 7 days of the experiment, which is not reflected in the model results, which is due to the detachment of the surface layer after soaking of the  $\text{Ca}(\text{OH})_2$  specimens. However, it should be noted that only the continuous dissolution is considered in this model.

#### 4.2 Parameter research

An exhaustive series of parametric studies was conducted to identify the effect of each parameter containing an actual physical significance on the model results. Firstly, the effect of the morphology of the crack on the healing effect was analyzed. The cracks are represented by two parallel sine waves. The surface roughness is constructed by adjusting the sinusoidal frequency. The amplitude of four cases is 2 and the frequencies are 1, 5, 10 and 20 respectively. As

the surface roughness increases, the precipitation fills first in the areas of greater curvature. Then the interface  $I_{\text{p-a}}$  gradually becomes flat. As seen in Fig. 6a1, case 4 is the first to be completely healed, while case 1 only reaches 0.8. From Fig. 6a3, it can be observed that the growth rate of self-healing ratio keeps increasing until 0.04 s, while it gradually decreases afterwards, which makes the four curves almost parallel after 0.5 s (in Fig. 6a2). This is due to the curved interface which migrates spontaneously toward the center of the curvature. The larger the curvature of the interface, the smaller the radius of the curvature, the faster the interface migration, and the faster the interface will move.

The rate of the interface migration resulting from the thermodynamic driving force of precipitation and dissolution is controlled by  $L_i$ . In this model,  $L_{\text{SOu}}^*$  and  $L_{\text{pre}}^*$  is referring to the normalized interface mobility coefficient of  $I_{\text{s-p}}$  and  $I_{\text{p-a}}$ , respectively. Figure 6b1 shows snapshots of crack simulations with three coefficient ratios ( $L_{\text{pre}}^*/L_{\text{SOu}}^* = 1, 10$  and  $100$ ) at  $0.3t^*$  and  $0.6t^*$ . It is obvious that when the coefficient ratio increases from 1 to 100, the self-healing ratio increases (Fig. 6b2) while the residual source phase ratio decreases (Fig. 6b3) significantly.

In order to simulate the physicochemical reactions correctly, the thickness of the interface has to be sufficiently small compared to the mesoscopic structure of the system; however, from a computational point of view, it is expected that the thickness of the interface has to be as large as possible in order to keep the interface from being overly densely meshed, which increases the computational effort. Therefore, for the simulation of crack healing with sinusoidal morphology, we quantitatively evaluated the effect of different interfacial widths ( $l_{i-j} = 1, 2$  and  $4$ ) on the model behavior. Figure 6c1 shows that the operating state of sinusoidal cracks is sensitive to the interface thickness. It is evident that when the interface thickness is 1, there is a clear boundary between the two phases. And when the interfacial thickness increases to 4, the interface morphology becomes blurred. Figure 6c2 shows the spatial distribution of  $\phi_{\text{pre}}$  at  $0.25t^*$  along the dashed line. As the interfacial width increases, the value of  $\phi_{\text{pre}}$  at the crack location becomes larger, which implies that the cracks can heal faster.

So far, for all simulations the same diffusion coefficient was assumed for each phase. Therefore,



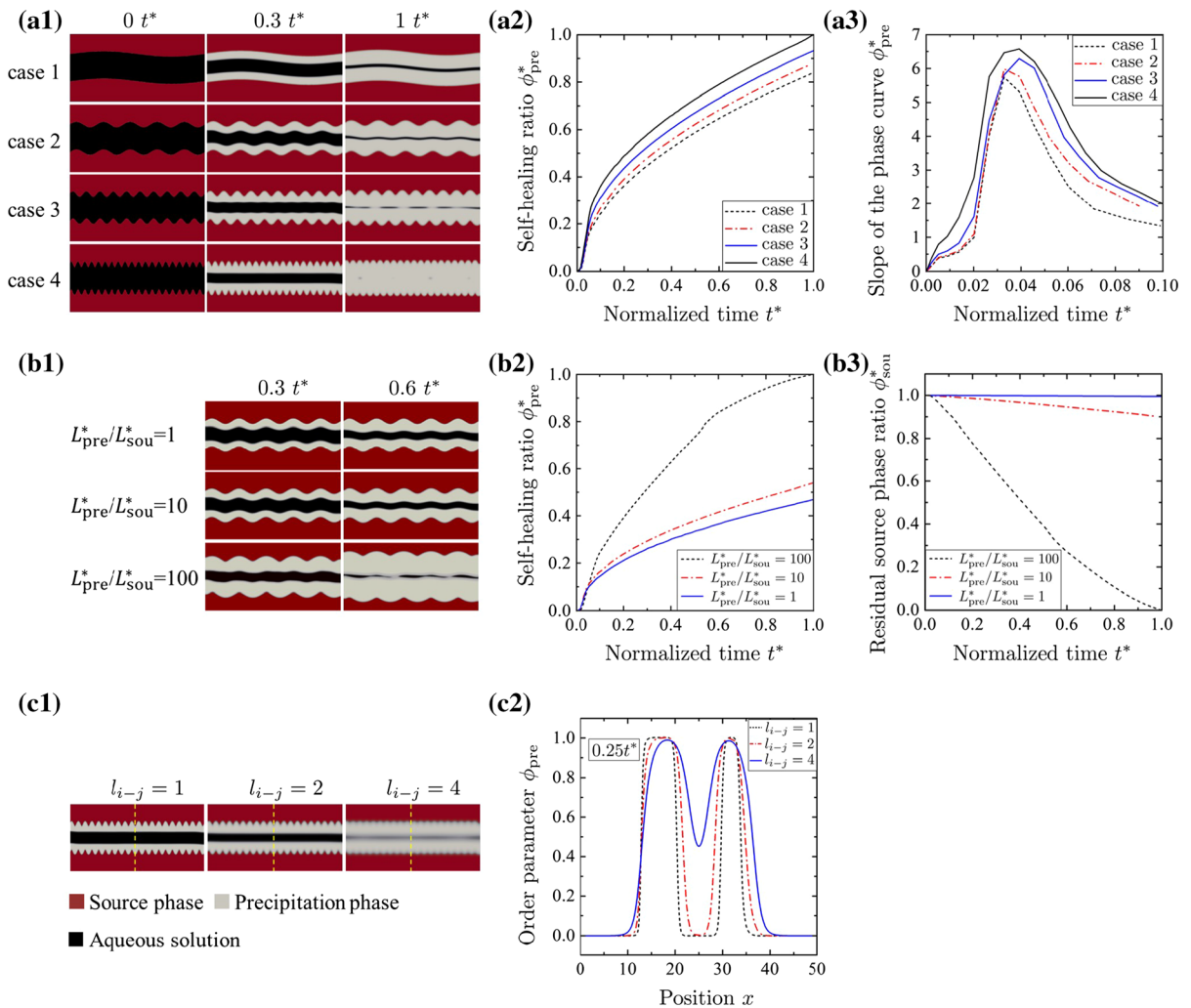


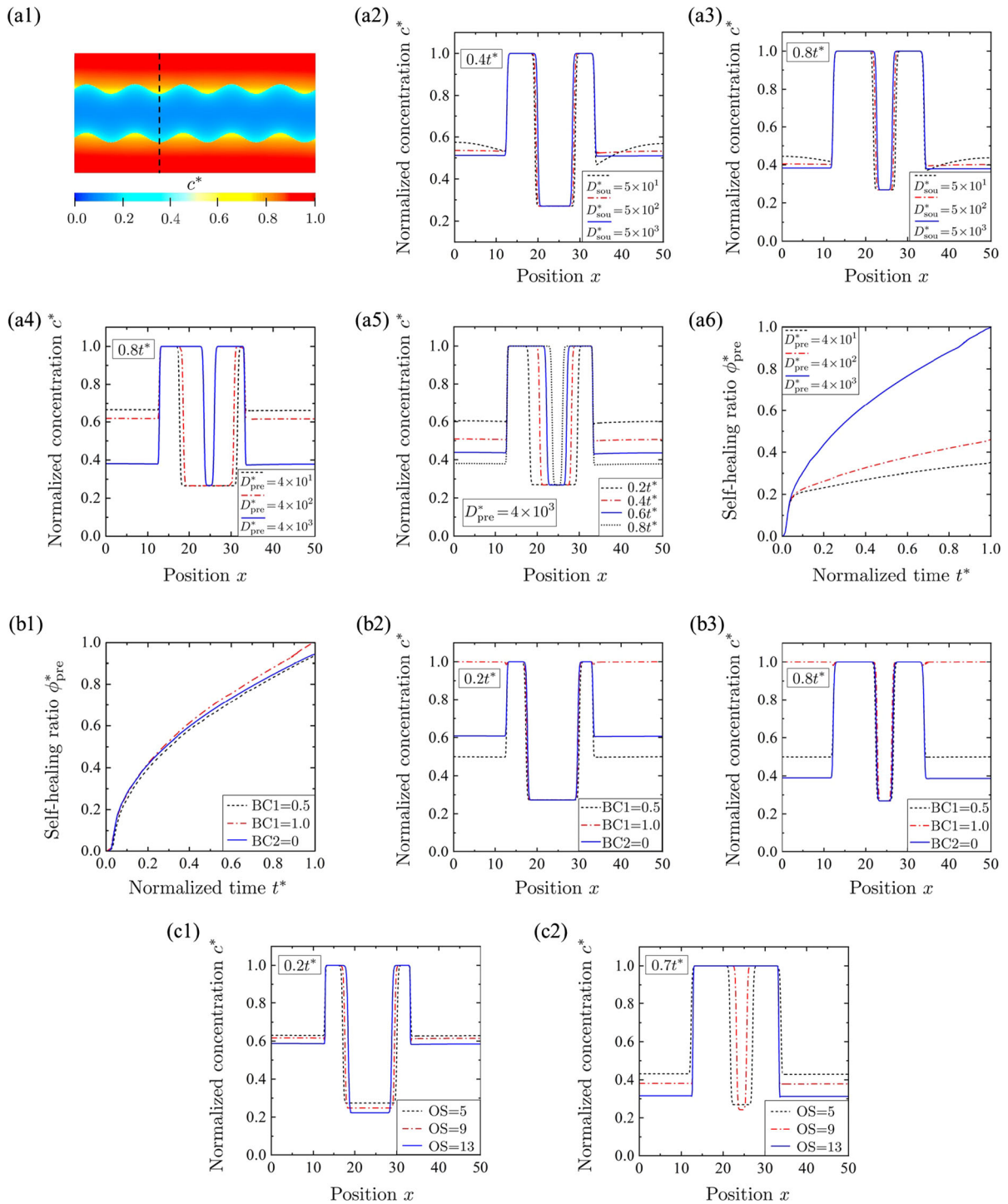
**Fig. 6** The effect PF parameter on profile of OP  $\{\phi_i\}$ . **a1** Simulation of self-healing with different crack morphologies, **a2, a3** the evolution of normalized phase ratio and its slope; **b1** Evolution of self-healing with variation of interface mobility

coefficient  $L_i$ , **b2, b3** normalized phase ratio  $\phi_{pre}^*$  and normalized phase ratio  $\phi_{sou}^*$  as a function of time, respectively; Effect of interfacial width and **c2** phase  $\phi_{shp}$  profile evolution

the performance of the model will be tested when varying the effective diffusion coefficient of ions in the source phase  $D_{sou}^*$  and that in the precipitation phase  $D_{pre}^*$ . All of them are normalized ( $D_{sou}^* = 5 \times 10^1, 5 \times 10^2$  and  $5 \times 10^3$ ;  $D_{pre}^* = 4 \times 10^1, 4 \times 10^2$  and  $4 \times 10^3$ ) with  $D_{aq} = 1 \times 10^{-9}$  m<sup>2</sup>/s (see Table 1, Sect. 3.1.2). Figure 7a2 shows that the concentration profile of  $D_{sou}^* = 5 \times 10^1$  is higher compared to that of  $D_{sou}^* = 5 \times 10^2$  and  $D_{sou}^* = 5 \times 10^3$  at  $0.4t^*$  in the ion source phase and clearly decreases from the boundary of the ion source phase to the fracture surface, especially with a low concentration

spike at  $x = 34$ . This is due to the large difference between  $D_{sou}^*$  and  $D_{pre}^*$ , which drives the ions appearing at the crack surface to diffuse rapidly into the precipitation region forming a concentration depletion zone at the crack surface. At  $0.8t^*$  (Fig. 7a3) the concentration spike rises due to more ions being transported to the fracture surface, thus compensating for the local concentration depletion. Figure 7a4 presents that the high concentration region ( $c^*=1$ ) widened significantly with increasing  $D_{pre}^*$ . Higher  $D_{pre}^*$  promotes rapid ion abstraction from the source phase, which causes the concentration to decrease with





◀ **Fig. 7** The effect PF parameter on profile of concentration  $c_i$ . **a1** The position of the studied profiles, **a2, a3** the distribution profiles of  $c^*$  at  $0.4t^*$  and  $0.8t^*$  with the variation of  $D_{\text{Sou}}^*$ , respectively, **a4** the distribution profiles of  $c^*$  at  $0.8t^*$  with the variation of  $D_{\text{pre}}^*$ , **a5** the distribution profiles of  $c^*$  of the case  $D_{\text{pre}}^* = 4 \times 10^3$  at four time points, **a6** the evolution of the normalized phase ratio  $\phi_{\text{pre}}^*$  with the variation of  $D_{\text{pre}}^*$ ; **b1** Evolution of self-healing ratio  $\phi_{\text{shp}}^*$  with different boundary conditions, normalized concentration profile evolution **b2** at  $0.2t^*$  and **b3** at  $0.8t^*$ ; Evolution of normalized concentration profile with the different oversaturation terms  $\Delta_{\text{rf}}$  at **c1**  $0.2t^*$  and **c2**  $0.7t^*$

increasing  $D_{\text{pre}}^*$  in the ion source phase. Figure 7a5 shows the concentration profiles from  $0.2t^*$  to  $0.8t^*$  for  $D_{\text{pre}}^* = 4 \times 10^3$ . Combining Fig. 7a5, a6, it can be observed that the expansion of the high concentration region ( $c^* = 1$ ) slows down with time which leads to a decrease in the precipitation phase  $\phi_{\text{pre}}^*$ . The above results indicate that an increase in the effective diffusivity of ions produces a significant increase in the precipitation width. It is worth emphasizing that in the PF method the order parameter and the concentration field are defined based on the mean field theory, which means that the fluctuated property of the concentration coefficients in the same phase are homogenized and therefore represented by a constant value. For the case where the mass transfer (incl. diffusion and fluid transfer) depending on the local pore structures, an additional conserved order parameter and corresponding fluid dynamics should be implemented [75].

The effect of two boundary conditions (BC1 and BC2) on the self-healing efficiency is discussed next. Under BC1, the effects caused by ion concentrations of 0.5 and 1.0 are compared. The position of the studied profiles is shown in Fig. 7a1. Figure 7b investigates the self-healing ratio  $\phi_{\text{pre}}^*$  and normalized concentration profiles  $c_i^*$  with the above boundary conditions. As shown in Fig. 7b1, when the constant concentration  $c_0^*$  of the boundary (Fig. 3) is increased from 0.5 to 1.0, the ratio of self-healing increases. As time increases from  $0.2t^*$  to  $0.8t^*$ , there is no change in the concentration profiles in the source phase in case of boundary with a constant concentration. In contrast, the normalized ion concentration in the source phase under BC2 decreases from 0.61 to 0.39 due to further

diffusion of calcium ions from the boundary to the crack surface (Fig. 7b2, b3).

Since it is not clear whether and how the precipitation reaction term  $\Delta_{\text{rf}}$  affects the concentration profiles, the effect of three cases  $\Delta_{\text{rf}} = 5, 9$  and 13 will be discussed now. The results in Fig. 7c1, c2 indicates a strong dependence of the concentration profiles on  $\Delta_{\text{rf}}$ . Changing  $\Delta_{\text{rf}}$  from 5 to 13 produces a significant decrease of the ion concentration in the source and solution phase, which finally results in a wider precipitation region. From  $0.2t^*$  to  $0.7t^*$ , all depressions in the middle of the curve with OS = 13 are replaced by a high concentration, indicating that the crack is completely healed. The driving force contributed by  $\Delta_{\text{rf}}$  drives the ions to diffuse from the source phase into the solution eventually accumulating at the crack surface. As a result, the ion concentration in the source phase and solution decreases rapidly, while the high concentration region in the phase with self-healing products increases. The above results show that the precipitation reaction progress can be effectively controlled by adjusting  $\Delta_{\text{rf}}$ .

#### 4.3 Modeling applications

The following two examples (Fig. 8) demonstrate that the PF model can be used to quantitatively simulate the morphological migrations of self-healing cementitious materials. Example 1 is the autogenous self-healing studied by Lee and Ryou [16], while example 2 is bacteria-based self-healing studied by Erşan et al. [76]. The reasons for choosing these two examples are as follows. First of all, the primary mechanism of the autogenous self-healing is the crystallization of  $\text{CaCO}_3$  [77]. Secondly, the principle mechanism of bacterial self-healing is that the bacteria act primarily as catalysts, and convert the organic biomineral precursor compound into insoluble inorganic  $\text{CaCO}_3$  based minerals [78–81]. When bacteria control the catalytic reaction much faster than diffusion, the self-healing process is mainly controlled by diffusion. In conclusion, these two examples can be numerically treated as a dissolution and precipitation process of solutes, which is time-dependent and controlled by diffusion. Therefore, both can be simulated using the PF model proposed in this study.

The initial widths of examples 1 and 2 are taken from the experimental data, i.e., 174  $\mu\text{m}$  and 318  $\mu\text{m}$ , respectively. The model parameters are the same as

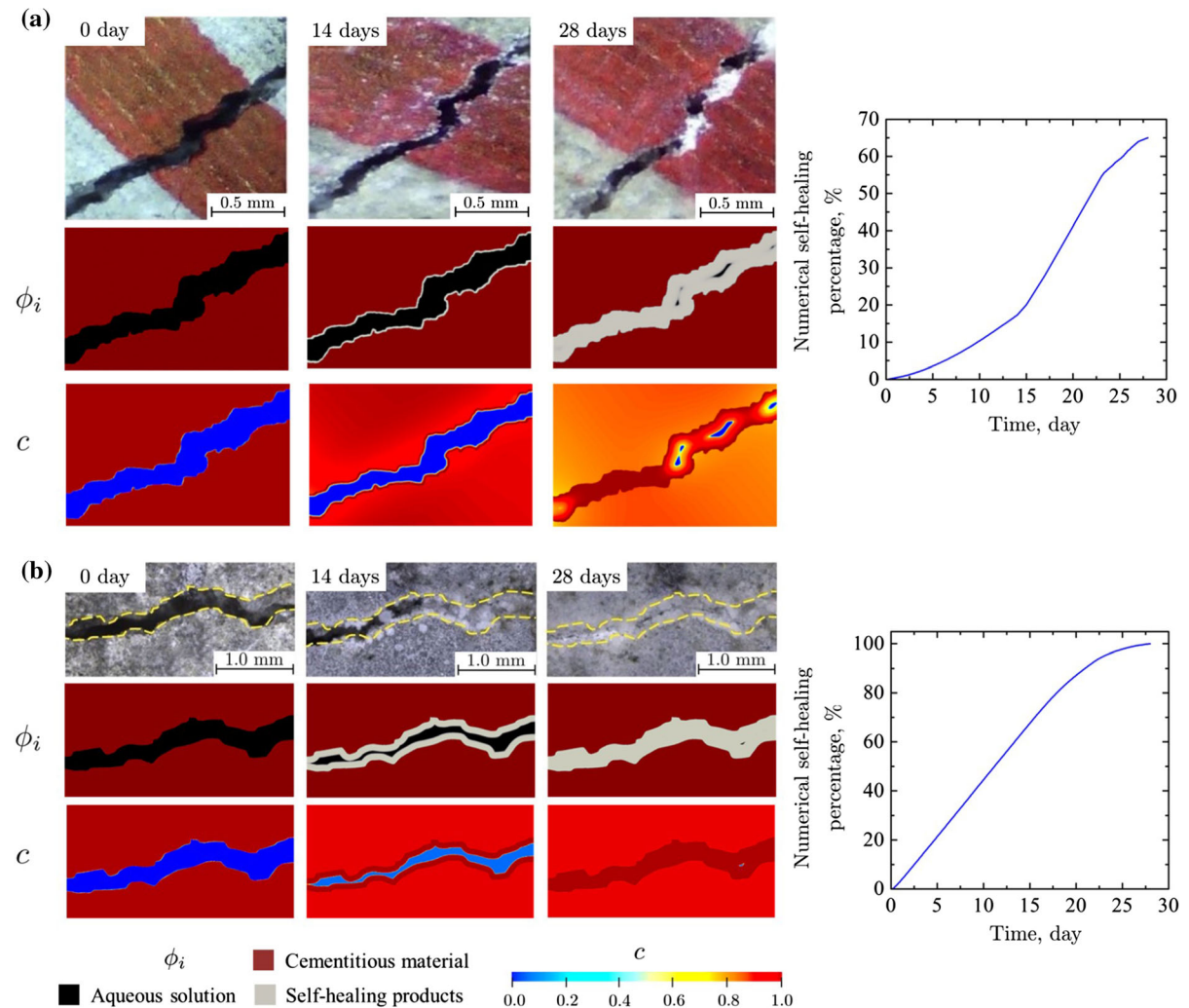


**Fig. 8** Two examples demonstrating the practical application of the PF model. **a** Example 1: the autogenous self-healing, reproduced with permission from the authors of [16], copyright

2014, Constr Build Mater, Elsevier; **b** example 2: the bacteria-based self-healing, reproduced with permission from the authors of [76], copyright 2016, Cem Concr Compos, Elsevier

that in Table 2 except  $L_{aq} = 1 \times 10^{-7} \text{ m}^3/(\text{Js})$ ,  $L_{pre} = 1 \times 10^{-4} \text{ m}^3/(\text{Js})$  and  $L_{sou} = 1 \times 10^{-10} \text{ m}^3/(\text{Js})$  used for example 1 and  $L_{aq} = 1 \times 10^{-5} \text{ m}^3/(\text{Js})$ ,  $L_{pre} = 1 \times 10^{-4} \text{ m}^3/(\text{Js})$  and  $L_{sou} = 1 \times 10^{-10} \text{ m}^3/(\text{Js})$  used for example 2, respectively. The precipitation reaction term  $\Delta_{rf}$  is an expression of the free energy density related to the chemical formation of  $\text{CaCO}_3$  particles (Eq. 6). In this PF model, we simplify the precipitation term to a non-negative constant. Based on the authors' research experience, a reasonable range of values for  $\Delta_{rf}$  is from 1 to 20. In order to focus on the effect of other parameters on the self-healing effect and to avoid the

model being subjected to a large  $\Delta_{rf}$  that would lead to too rapid healing,  $\Delta_{rf}$  was taken as 5 in both examples.

Figure 8 shows schematically the concentration field  $c$ , the phase field  $\phi_i$  and the experimental results for the 2 examples at different times, respectively. At the beginning of cracking, the reactant ion concentration  $c$  is highest in the cementitious matrix and nearly 0 in the solution. At 14 days,  $c$  at the crack surface reaches 1, while a layer of self-healing products. This indicates that the  $\text{Ca}^{2+}$  ions in the solution are carbonated and the concentration of  $\text{CaCO}_3$  reaches the saturation state forming a layer of self-healing products. The concentration in the cementitious matrix

is low compared to that on the crack surface. Such a difference is set to numerically reflect a physical meaning, i.e.,  $\text{CaCO}_3$  precipitation is difficult to form in the deep cementitious matrix due to the lack of  $\text{CO}_2$ . It can be carbonated only when  $\text{Ca}^{2+}$  ions diffuse to the crack surface. It is one of the innovations of our model that  $c$  can reach 1 only near the crack surface, thus allowing the formation of the self-healing products locally. With this strategy, the different phases can be effectively distinguished by their concentrations and tracked by the corresponding order parameters.

It is clear from the experimental results that the morphology of the cracks largely influences their local healing effect. At the same time the morphology of the crack is constantly changing with the healing process. In the depression out of the crack surface, the healing products precipitate faster and more frequently due to the higher concentration of solutes. Therefore, its local boundary moves faster than that of other locations.

The effect of crack width on the self-healing efficiency can also be seen in the simulation results of examples 1 and 2. This effect has also been mentioned in the literature [82, 83]. From the simulation results of example 1, it can be seen that the crack healing rate from 0 to 15 days is slower than that from 15 to 23 days. This is due to the slow diffusion process of  $\text{Ca}^{2+}$  ions from the cement matrix to the crack surface and their gradual accumulation in the early stage of crack appearance. Precipitation occurs only when ions concentration reaches the saturation state. The results from days 0–15 reflect the gradual accumulation of reactant concentrations. After 15 days, the crack healing rate is accelerated. This is due to the synergistic effect of  $\text{Ca}^{2+}$  ions diffusing from both crack sides. However, the width of example 2 is 1.8 times wider than that of example 1, which leads to the fact that the processes of diffusion of  $\text{Ca}^{2+}$  ions and occurrence of precipitation reactions on both sides of the crack are independent of each other and have no synergistic effect. Therefore the self-healing rate of example 2 was almost constant until 20 days. The self-healing rates of the two examples slowed down after 23 and 20 days, respectively. This is due to the formation of a  $\text{CaCO}_3$  layer on the crack surface thereby preventing further diffusion of  $\text{Ca}^{2+}$  ions outward.

The above two numerical simulations provides consistent results with experiments, which is encouraging as for the capacity of the present model to predict the morphology and the geometrical details of the interface migration of self-healing processes in cementitious materials. However, we should keep in mind that the comparison between numerical and experimental results is mainly qualitative, since we have focused only on the dissolution–precipitation mechanism, whereas for cementitious materials containing mineral additives, the corresponding self-healing processes have to be extended to consider more types of reactions (e.g. hydration) and additional physicochemical effects (e.g. swelling and dissolution). In addition, although the empirical relationship between effective diffusivity and porosity (single value) takes into account the effect of w/c ratio, the variation of porosity is not studied in this study. The porosity should be related to the local concentration of ions and the phase in which they are located. The diffusion coefficient could be expressed as an equation related to the porosity and pore structure [68]. This model can be flexibly extend to a multiphase multi-component form to analyze the effect of real cementitious materials on self-healing, e.g., by adding a order parameter  $\phi_{\text{sou\_csh}}$  for C-S-H in the phase of  $\phi_{\text{sou}}$ . For this, a thermodynamic dissolution-precipitation description should be implemented as well as a change of the homogenized properties. The fluctuated properties should be homogenized and generally represented by a non-constant value, where e.g. the effective diffusion coefficient depends on the pore structure (e.g. using empirical relations [53, 68]).

## 5 Conclusion

In this study, a novel PF model for self-healing of cementitious materials is presented. The model can effectively capture the evolution of dissolution and precipitation interfaces controlled by diffusion and the behavior of solute concentration profiles. From the results of this study following conclusion can be drawn:

- (1) The free energy of the system, approximated by a set of parabolic functions, varies with solute concentrations and order parameters, which is able to describe the self-healing processing by

analyzing the thermodynamic driving force of the solute diffusion and precipitation in a thermodynamic-consistent way and thereby capable in recapitulating the process under various solute conditions, i.e. undersaturation, saturation and oversaturation;

- (2) Calcium hydroxide-based carbonation measurements confirm that multiple interface evolution occurs during the self-healing process. Using the derived interfacial mobility, the PF numerical simulations show a consistent agreement with the experimental results;
- (3) By conducting a series of parametric studies, it was confirmed that model parameters with clear physical meanings can reflect the evolution of multiple interfaces under different conditions;
- (4) 2D simulations of the interfacial growth kinetics during the self-healing of cementitious materials were carried out. Comparison with experimental results shows that the PF model is able to provide good qualitative predictions of the morphological and geometric details of interfacial migration during self-healing of cementitious materials in terms of minerals dissolution and precipitation (Fig. 8). For a further quantitative analysis, additional types of chemical reactions and additional physical factors need to be considered.

In future studies, the free energies and the corresponding thermodynamic parameters of the involved phases will be examined to quantify mechanisms for the formation of the self-healing products, e.g. hydration kinetics, crystallization kinetics and swelling. Due to the dependence on the ion type, ion concentration, capillary pore structure, degree of chemical reaction, etc. an explicit formulation of the diffusion coefficient on relevant factors shall be derived and validated with experiments [84]. The chemistry modeling should be extended with the  $\text{Ca}^{2+}$  ion diffusion coefficient to be subject to the interaction of porosity and chemical reaction rate. Ion transport and local chemical reactions can be calculated using PHREEQC (a computer program for speciation, reaction-path, advective transport, and inverse geochemical calculations). The yielded results are then transferred to the PF model for the further phase transformation analysis. The complex evolution of crack healing morphology in physicochemical processes can be accurately

evaluated only in a full 3D system. All the above should be considered for further development of a comprehensive self-healing modeling tool for cementitious materials.

**Acknowledgements** The authors in TU Darmstadt acknowledge the support by the EU-funded cost action “CA15202—Self-healing As preventive Repair of Concrete Structures”. Calculations for this research were conducted on the Lichtenberg high performance computer of the TU Darmstadt.

**Author contributions** Conceptualization: Sha Yang and Antonio Caggiano; Methodology: Sha Yang and Yangyiwei Yang; Experiment: Sha Yang; Writing—original draft preparation: Sha Yang; Writing—review and editing: everybody; Supervision: Antonio Caggiano and Neven Ukrainczyk; Project administration: Eddie Koenders; Funding acquisition: Eddie Koenders. All authors have read and agreed to the published version of the manuscript.

**Funding** Open Access funding enabled and organized by Projekt DEAL. This research was funded by National German DFG organization: (i) under Project No. 387065993 titled “Form filling ability of fresh concrete: A time and hydration dependent approach”, as part of DFG SPP 2005 program “Opus Fluidum Futurum—Rheology of reactive, multiscale, multiphase construction materials”; and (ii) under project number 426807554 titled “Experimentally supported multi-scale Reactive Transport modeling of cementitious materials under Acid attack (ExpeRTa)”.

#### Declarations

**Conflict of interest** The authors declare that they have no conflict of interest.

**Open Access** This article is licensed under a Creative Commons Attribution 4.0 International License, which permits use, sharing, adaptation, distribution and reproduction in any medium or format, as long as you give appropriate credit to the original author(s) and the source, provide a link to the Creative Commons licence, and indicate if changes were made. The images or other third party material in this article are included in the article’s Creative Commons licence, unless indicated otherwise in a credit line to the material. If material is not included in the article’s Creative Commons licence and your intended use is not permitted by statutory regulation or exceeds the permitted use, you will need to obtain permission directly from the copyright holder. To view a copy of this licence, visit <http://creativecommons.org/licenses/by/4.0/>.

#### References

1. Kumar MP, Burrows Richard W (2001) Building durable structures in the 21st century. *Concr Int* 23(3):57–63





2. Tang SW, Yao Y, Andrade C, Li ZJ (2015) Recent durability studies on concrete structure. *Cem Concr Res* 78:143–154
3. Saito M, Ohta M, Ishimori H (1994) Chloride permeability of concrete subjected to freeze–thaw damage. *Cement Concr Compos* 16(4):233–239
4. Hilsdorf H, Kropp Jörg (1995) Performance criteria for concrete durability. CRC Press, London
5. Song H-W, Kwon S-J, Byun K-J, Park C-K (2006) Predicting carbonation in early-aged cracked concrete. *Cem Concr Res* 36(5):979–989
6. Chang C-F, Chen J-W (2006) The experimental investigation of concrete carbonation depth. *Cem Concr Res* 36(9):1760–1767
7. Ferrara L, Van Mullem T, Alonso MC, Antonaci P, Borg RP, Cuenca E, Jefferson A, Ng P-L, Peled A, Roig-Flores M et al (2018) Experimental characterization of the self-healing capacity of cement based materials and its effects on the material performance: A state of the art report by cost action sarcos wg2. *Constr Build Mater* 167:115–142
8. Van Tittelboom K, De Belie N (2013) Self-healing in cementitious materials—a review. *Materials* 6(6):2182–2217
9. De Belie N, Gruyaert E, Al-Tabbaa A, Antonaci P, Baera C, Bajare D, Darquennes A, Davies R, Ferrara L, Jefferson T et al (2018) A review of self-healing concrete for damage management of structures. *Adv Mater Interfaces* 5(17):1800074
10. Sisomphon K, Copuroglu O, Koenders EAB (2012) Self-healing of surface cracks in mortars with expansive additive and crystalline additive. *Cement Concr Compos* 34(4):566–574
11. Wang JY, Snoeck D, Van Vlierbergh S, Verstraete W, De Belie N (2014) Application of hydrogel encapsulated carbonate precipitating bacteria for approaching a realistic self-healing in concrete. *Constr Build Mater* 68:110–119
12. De Rooij M, Van Tittelboom K, De Belie N, Schlagen E (2013) Self-healing phenomena in cement-Based materials: state-of-the-art report of RILEM technical committee 221-SHC: self-Healing phenomena in cement-Based materials, volume 11. Springer
13. Huang H, Ye G, Damidot D (2013) Characterization and quantification of self-healing behaviors of microcracks due to further hydration in cement paste. *Cem Concr Res* 52:71–81
14. Yang Y, Yang E-H, Li VC (2011) Autogenous healing of engineered cementitious composites at early age. *Cem Concr Res* 41(2):176–183
15. Hilloulin B, Van Tittelboom K, Gruyaert E, De Belie N, Loukili A (2015) Design of polymeric capsules for self-healing concrete. *Cement Concr Compos* 55:298–307
16. Lee Y-S, Ryou J-S (2014) Self healing behavior for crack closing of expansive agent via granulation/film coating method. *Constr Build Mater* 71:188–193
17. Seifan M, Berenjian A (2018) Application of microbially induced calcium carbonate precipitation in designing bio self-healing concrete. *World J Microbiol Biotechnol* 34(11):1–15
18. Aliko-Benítez A, Doblare M, Sanz-Herrera JA (2015) Chemical-diffusive modeling of the self-healing behavior in concrete. *Int J Solids Struct* 69:392–402
19. Yang S, Caggiano A, Yi M, Ukrainczyk N, Koenders EAB (2019) Modelling autogenous self-healing with dissoluble encapsulated particles using a phase field approach. In: *Mecánica Computacional*, pp 1457–1467
20. Di Luzio G, Ferrara L, Krelani V (2014) A numerical model for the self-healing capacity of cementitious composites. In: *Proceedings of the computational modelling of concrete structures*, St. Anton am Arlberg, Austria, pp 24–27
21. Silviana CA, Duncan JA (2016) A coupled thermo-hydro-chemical model for characterising autogenous healing in ordinary cementitious materials. *Cem Concr Res* 88:184–197
22. Lv Z, Chen H (2012) Modeling self-healing efficiency on cracks due to unhydrated cement nuclei in cementitious materials: splitting crack mode. *Sci Eng Compos Mater* 19(1):1–7
23. Hilloulin B, Grondin F, Matallah M, Loukili A (2014) Modelling of autogenous healing in ultra high performance concrete. *Cem Concr Res* 61:64–70
24. He H, Guo Z-Q, Stroeven P, Hu J, Stroeven M (2007) Computer simulation study of concrete’s self-healing capacity due to unhydrated cement nuclei in interfacial transition zones. In: *Proc 1st Int Conf Self-healing materials*. Noordwijk aan Zee, The Netherlands, volume 51
25. He H, Guo Z, Stroeven P, Stroeven M, Sluys LJ (2007) Self-healing capacity of concrete-computer simulation study of unhydrated cement structure. *Image Anal Stereol* 26(3):137–143
26. Ferrara Liberato DI, Giovanni LUZIO, Visar K et al (2016) Experimental assessment and numerical modeling of self healing capacity of cement based materials via fracture mechanics concepts. In *FraMCoS* 9:1–12
27. Zemskov SV, Jonkers HM, Vermolen FJ (2014) A mathematical model for bacterial self-healing of cracks in concrete. *J Intell Mater Syst Struct* 25(1):4–12
28. Lv Z, Chen H (2013) Analytical models for determining the dosage of capsules embedded in self-healing materials. *Comput Mater Sci* 68:81–89
29. Zhu H, Zhou S, Yan Z, Woody J, Chen Q (2015) A 3d analytical model for the probabilistic characteristics of self-healing model for concrete using spherical microcapsule. *Comput Concr* 15(1):37–54
30. Huang H, Ye G (2016) Numerical studies of the effects of water capsules on self-healing efficiency and mechanical properties in cementitious materials. In: *Advances in materials science and engineering* (2016)
31. Zhou S, Hehua Zhu J, Woody J, Yan Z, Chen Q (2017) Modeling microcapsule-enabled self-healing cementitious composite materials using discrete element method. *Int J Damage Mech* 26(2):340–357
32. Huang H, Ye G (2012) Simulation of self-healing by further hydration in cementitious materials. *Cement Concr Compos* 34(4):460–467
33. Ying Y, Urban Marek W (2013) Self-healing polymeric materials. *Chem Soc Rev* 42(17):7446–7467
34. Chen J, Ye G (2019) A Lattice Boltzmann single component model for simulation of the autogenous self-healing caused by further hydration in cementitious material at mesoscale. *Cem Concr Res* 123:105782

35. Muntean A (2006) A moving-boundary problem: modeling, analysis and simulation of concrete carbonation. Cuvillier Verlag
36. Adrian M, Böhm M, Kropp J (2011) Moving carbonation fronts in concrete: a moving-sharp-interface approach. *Chem Eng Sci* 66(3):538–547
37. Zheng M, Liu F, Liu Q, Burrage K, Simpson MJ (2017) Numerical solution of the time fractional reaction–diffusion equation with a moving boundary. *J Comput Phys* 338:493–510
38. Peter MA, Muntean A, Meier SA, Böhm M (2008) Competition of several carbonation reactions in concrete: a parametric study. *Cem Concr Res* 38(12):1385–1393
39. Yang Y, Kühn P, Yi M, Egger H, Bai-Xiang X (2020) Non-isothermal phase-field modeling of heat-melt-microstructure-coupled processes during powder bed fusion. *JOM* 72(4):1719–1733
40. Zhijie X, Meakin P (2008) Phase-field modeling of solute precipitation and dissolution. *J Chem Phys* 129(1):014705
41. Zhijie X, Huang H, Li X, Meakin P (2012) Phase field and level set methods for modeling solute precipitation and/or dissolution. *Comput Phys Commun* 183(1):15–19
42. TL Van Noorden and Christof Eck (2011) Phase field approximation of a kinetic moving-boundary problem modelling dissolution and precipitation. *Interfaces Free Bound* 13(1):29–55
43. Redeker M, Rohde C, Pop IS (2016) Upscaling of a tri-phase phase-field model for precipitation in porous media. *IMA J Appl Math* 81(5):898–939
44. Wang Y, Chen L-Q, Khachatryan AG (1993) Kinetics of strain-induced morphological transformation in cubic alloys with a miscibility gap. *Acta Metall Mater* 41(1):279–296
45. Rubin G, Khachatryan AG (1999) Three-dimensional model of precipitation of ordered intermetallics. *Acta Mater* 47(7):1995–2002
46. Chen Q, Ma N, Kaisheng W, Wang Y (2004) Quantitative phase field modeling of diffusion-controlled precipitate growth and dissolution in Ti–Al–V. *Scr Mater* 50(4):471–476
47. Wen Y-H, Chen L-Q, Hawk JA (2012) Phase-field modeling of corrosion kinetics under dual-oxidants. *Modell Simul Mater Sci Eng* 20(3):035013
48. Mai W, Soghrati S (2018) New phase field model for simulating galvanic and pitting corrosion processes. *Electrochim Acta* 260:290–304
49. Abdulhamid AA, Sohail AS, Arif AFM (2015) Phase field modeling of  $v_2o_5$  hot corrosion kinetics in thermal barrier coatings. *Comput Mater Sci* 99:105–116
50. Huang H (2014) Thermodynamics of autogenous self-healing in cementitious materials
51. Sulapha P, Wong SF, Wee TH, Swaddiwudhipong S (2003) Carbonation of concrete containing mineral admixtures. *J Mater Civ Eng* 15(2):134–143
52. Zhu Yu, Yang Y, Yao Y (2012) Autogenous self-healing of engineered cementitious composites under freeze–thaw cycles. *Constr Build Mater* 34:522–530
53. Tri PQ, Norbert M, Diederik J, Geert DS, Guang Y, Janez P (2016) Modelling the carbonation of cement pastes under a CO<sub>2</sub> pressure gradient considering both diffusive and convective transport. *Constr Build Mater* 114:333–351
54. Allain C, Cloitre M, Wafra M (1995) Aggregation and sedimentation in colloidal suspensions. *Phys Rev Lett* 74(8):1478
55. Lu PJ, Zaccarelli E, Ciulla F, Schofield AB, Sciortino F, Weitz DA (2008) Gelation of particles with short-range attraction. *Nature* 453(7194):499–503
56. Schwen D, Aagesen LK, Peterson JW, Tonks MR (2017) Rapid multiphase-field model development using a modular free energy based approach with automatic differentiation in moose/marmot. *Comput Mater Sci* 132:36–45
57. Tóth GI, Pusztai T, Gránásy L (2015) Consistent multiphase-field theory for interface driven multidomain dynamics. *Phys Rev B* 92(18):184105
58. Petersen T, Valdenaire P-L, Pellenq R, Ulm F-J (2018) A reaction model for cement solidification: evolving the c–s–h packing density at the micrometer-scale. *J Mech Phys Solids* 118:58–73
59. Kim SG, Kim WT, Suzuki T (1999) Phase-field model for binary alloys. *Phys Rev E* 60(6):7186
60. Allen SM, Cahn JW (1979) A microscopic theory for anti-phase boundary motion and its application to antiphase domain coarsening. *Acta Metall* 27(6):1085–1095
61. Gaston D, Newman C, Hansen G, Lebrun-Grandie D (2009) Moose: A parallel computational framework for coupled systems of nonlinear equations. *Nucl Eng Des* 239(10):1768–1778
62. Loo YH, Chin MS, Tam CT, Ong KCG (1994) A carbonation prediction model for accelerated carbonation testing of concrete. *Mag Concr Res* 168(46):191–200
63. Cui H, Tang W, Liu W, Dong Z, Xing F (2015) Experimental study on effects of CO<sub>2</sub> concentrations on concrete carbonation and diffusion mechanisms. *Constr Build Mater* 93:522–527
64. Liu W, Li Y-Q, Tang L-P, Dong Z-J (2019) XRD and 29Si MAS NMR study on carbonated cement paste under accelerated carbonation using different concentration of CO<sub>2</sub>. *Mater Today Commun* 19:464–470
65. Loste E, Díaz-Martí E, Zarbakhsh A, Meldrum FC (2003) Study of calcium carbonate precipitation under a series of fatty acid langmuir monolayers using brewster angle microscopy. *Langmuir* 19(7):2830–2837
66. Grafe U, Böttger B, Tiaden J, Fries SG (2000) Coupling of multicomponent thermodynamic databases to a phase field model: application to solidification and solid state transformations of superalloys. *Scr Mater* 42(12):1179–1186
67. Scheiner S, Hellmich C (2007) Stable pitting corrosion of stainless steel as diffusion-controlled dissolution process with a sharp moving electrode boundary. *Corros Sci* 49(2):319–346
68. Neven Ukrainczyk and EAB Koenders (2014) Representative elementary volumes for 3d modeling of mass transport in cementitious materials. *Modell Simul Mater Sci Eng* 22(3):035001
69. Yang S, Ukrainczyk N, Caggiano A, Koenders E (2021) Numerical phase-field model validation for dissolution of minerals. *Appl Sci* 11(6):2464
70. Fernandez-Martinez A, Yandi H, Lee B, Jun Y-S, Waychunas GA (2013) In situ determination of interfacial energies between heterogeneously nucleated CaCo<sub>3</sub> and quartz substrates: thermodynamics of co<sub>2</sub> mineral trapping. *Environ Sci Technol* 47(1):102–109



71. Dong B, Yang L, Yuan Q, Liu Y, Zhang J, Fang G, Wang Y, Yan Y, Xing F (2016) Characterization and evaluation of the surface free energy for cementitious materials. *Constr Build Mater* 110:163–168
72. Caré S, Hervé E (2004) Application of an-phase model to the diffusion coefficient of chloride in mortar. *Transp Porous Media* 56(2):119–135
73. Ribeiro Ana CF, Barros Marisa CF, Teles Ana SN, Valente Artur JM, Lobo Victor MM, Sobral Abílio JFN, Esteso MA (2008) Diffusion coefficients and electrical conductivities for calcium chloride aqueous solutions at 298.15 k and 310.15 k. *Electrochim Acta* 5(2):192–196
74. Coto Baudilio, Martos C, Peña JL, Rodríguez R, Pastor Gabriel (2012) Effects in the solubility of CaCo<sub>3</sub>: experimental study and model description. *Fluid Phase Equilib* 324:1–7
75. Yang Y, Ragnvaldsen O, Bai Y, Yi M, Xu B-X (2019) 3D non-isothermal phase-field simulation of microstructure evolution during selective laser sintering. *NPJ Comput Mater* 5(1):1–12
76. Erşan YÇ, Hernandez-Sanabria E, Boon N, De Belie N (2016) Enhanced crack closure performance of microbial mortar through nitrate reduction. *Cement Concr Compos* 70:159–170
77. Min W, Johannesson B, Geiker M (2012) A review: self-healing in cementitious materials and engineered cementitious composite as a self-healing material. *Constr Build Mater* 28(1):571–583
78. Jonkers HM, Schlangen E (2008) A two component bacteria-based self-healing concrete. In: Proceedings of the 2nd international conference on concrete repair, rehabilitation and retrofitting, pp 119–120
79. Wiktor V, Jonkers HM (2011) Quantification of crack-healing in novel bacteria-based self-healing concrete. *Cement Concr Compos* 33(7):763–770
80. Kua HW, Gupta S, Aday AN, Srubar III WV (2019) Bio-char-immobilized bacteria and superabsorbent polymers enable self-healing of fiber-reinforced concrete after multiple damage cycles. *Cem Concr Compos* 100:35–52
81. Whiffin VS, Van Paassen LA, Harkes MP (2007) Microbial carbonate precipitation as a soil improvement technique. *Geomicrobiol J* 24(5):417–423
82. Hung C-C, Su Y-F, Hung H-H (2017) Impact of natural weathering on medium-term self-healing performance of fiber reinforced cementitious composites with intrinsic crack-width control capability. *Cement Concr Compos* 80:200–209
83. Reinhardt H-W, Jooss M (2003) Permeability and self-healing of cracked concrete as a function of temperature and crack width. *Cem Concr Res* 33(7):981–985
84. Saetta AV, Vitaliani RV (2004) Experimental investigation and numerical modeling of carbonation process in reinforced concrete structures: Part I: Theoretical formulation. *Cem Concr Res* 34(4):571–579

**Publisher's Note** Springer Nature remains neutral with regard to jurisdictional claims in published maps and institutional affiliations.

